A unified stiffness evolution model and its application to 3D-printed regular and re-entrant honeycombs

Shaohua Wang*

Impact Mechanics Laboratory, Department of Mechanical Engineering, National University of Singapore, 9 Engineering Drive 1, Singapore, 117575, Singapore

Abstract

The evolution of the elastic modulus in cellular materials involves both post-yield stiffness degradation and densification-induced recovery, yet a unified theoretical framework to describe this non-monotonic behavior remains lacking. This study investigates the stiffness evolution and deformation mechanisms of regular hexagonal (HC) and re-entrant (NHC) honeycombs under quasi-static uniaxial compression. Specimens with varied wall thicknesses were fabricated using fused deposition modeling, and incremental loading–unloading tests were performed along two orthogonal in-plane directions. A stiffness evolution model was developed to describe the complete non-monotonic variation of the global modulus, incorporating a linear elastic pre-yield response within a modified rigid–plastic hardening framework. The model captures both stiffness degradation induced by localized collapse and subsequent recovery driven by structural compaction, outperforming conventional approaches that neglect modulus rebound. Pronounced anisotropy in modulus evolution is observed, governed by direction-dependent collapse mechanisms. Bending-dominated deformation in the 1-direction leads to progressive compaction and earlier stiffness recovery as wall thickness increases. In contrast, fracture-dominated crushing in the 2-direction delays the modulus rebound in thicker specimens due to enhanced structural strength and toughness. These results reveal that wall thickness not only scales the stiffness magnitude but also modulates its evolution path: thicker walls accelerate compaction in bending-dominated modes while delaying it in fracture-dominated modes. The proposed framework provides a robust theoretical foundation for the optimized design of honeycombs and offers predictive insights into the interplay between geometry, thickness, and performance evolution in architected materials.

Keywords: 3D printed honeycomb, Stiffness evolution, Incremental cyclic compression, Anisotropy, Collapse

*Corresponding author. Email: shwang@visitor.nus.edu.sg

1. Introduction

Honeycomb structures are widely utilized in engineering applications such as aerospace, automotive protection, and biomedical implants due to their exceptional strength-to-weight ratios and superior energy dissipation capacities [1–4]. Fused deposition modeling (FDM) has further expanded the design space for these materials, enabling the fabrication of complex architectures with tailored mechanical responses [5–7]. Despite these advances, the nonlinear evolution of the elastic modulus during compression remains insufficiently understood. In particular, a stiffness evolution model capable of describing the entire process from yielding to densification, together with the associated deformation mechanisms, is still lacking.

Honeycomb structures exhibit mechanical responses that are fundamentally governed by their topological configurations and deformation mechanisms [8–11]. Regular hexagonal honeycombs [12, 13], as systematically analyzed by Gibson and Ashby [14, 15], deform primarily through cell-wall bending or elastic buckling, depending on relative density, cell geometry, and loading direction. Their effective elastic modulus and initial yield strength can be derived from micromechanical beam theory, revealing clear scaling relationships with structural parameters [14–16]. In contrast, re-entrant honeycombs exhibit a negative Poisson's ratio arising from hinging-dominated deformation, leading to auxetic characteristics such as enhanced indentation resistance and improved shear stiffness [17–19]. With the emergence of fused deposition modeling (FDM), the fabrication of hexagonal and re-entrant honeycombs with controlled filament orientation and geometric anisotropy has become feasible, stimulating extensive experimental investigations [20–22]. Previous studies have examined the uniaxial compressive response of FDM-printed honeycombs under different in-plane loading angles, highlighting pronounced anisotropy in elastic stiffness, yield stress, and post-yield collapse modes [23, 24]. However, most existing works are limited to monotonic compression tests, which primarily capture global stress–strain behavior. Such approaches provide limited insight into the progressive stiffness degradation, recovery, or transition associated with cell-wall buckling, collapse, and densification. A comprehensive understanding of stiffness evolution therefore requires incremental loading–unloading experiments capable of decoupling elastic and plastic contributions throughout the deformation process.

Incremental loading–unloading experiments provide direct insight into damage accumulation and stiffness evolution during progressive compression and have therefore been widely adopted to evaluate the degradation and recovery behavior of cellular materials [25–31]. Flores-Johnson et al. [25] investigated the cyclic

compressive response of aluminum honeycombs and PVC foams, employing the instantaneous elastic modulus during compression as an indicator to quantify damage evolution. Their results revealed distinct material-dependent trends: polymeric foams exhibited pronounced post-yield stiffness degradation associated with cell-wall damage and collapse, whereas aluminum honeycombs showed negligible stiffness reduction and even a gradual increase in stiffness with increasing strain [25]. Finite element simulations at both the cell and continuum scales, in which intrinsic cell-wall material failure was not considered, similarly predicted a progressive stiffness increase during compression, primarily attributed to geometric compaction and cell-wall interactions [25, 32]. Recently, Wang et al. [33] conducted systematic incremental loading–unloading compression tests on polyurethane foams at different strain rates. It was demonstrated that the elastic modulus first decreases after yielding due to cell-wall fracture and crushing, followed by a subsequent increase induced by cell-wall contact and densification, as illustrated in Fig. 1. These apparently inconsistent findings collectively suggest that stiffness evolution in cellular solids is strongly governed by the interplay between intrinsic cell-wall material properties and cellular topology. Furthermore, for foamed materials with direction-dependent cell geometry, the stiffness evolution during compression has been shown to exhibit pronounced anisotropy [34–39]. However, in FDM-fabricated honeycombs, the stiffness evolution under compression for different unit-cell topologies such as regular hexagonal and re-entrant configurations, as well as under varying loading directions and wall thicknesses—has yet to be systematically elucidated.

Accurate constitutive modeling is essential for capturing the complex mechanical behavior of cellular solids under compression [15, 40–44]. Stress–strain relations derived from one-dimensional shock wave theory, such as the rigid– perfectly plastic–locking (R–PP–L) [45–47] and R–PH [48–53] formulations, typically adopt a rigid unloading assumption, thereby neglecting the elastic response during both loading and unloading stages. While these models are effective for describing high-rate compressive behavior, they are incapable of representing stiffness evolution throughout progressive deformation. Constitutive models based on elliptical yield surfaces have also been extensively developed for cellular materials [43, 44, 54, 55]. In most formulations, the elastic modulus is assumed to remain constant during compression, upon which isotropic [41], transversely isotropic [43, 44], and orthotropic [42, 56] models have been constructed. Such an assumption, however, precludes the description of stiffness degradation or recovery observed experimentally [25, 33]. To address densification-induced stiffening, Qiao et al. [32] introduced a stiffness enhancement mechanism to capture the transition from cellular compaction to fully dense material behavior, although systematic experimental validation remains limited. Conversely, Flores-Johnson et al. [25] proposed a stiffness degradation model based on progressive crushing assumptions; however, the model fails to account for the

stiffness increase reported in both experimental and numerical studies at large strains. Collectively, these limitations highlight the need for a physically consistent theoretical framework capable of simultaneously describing post-yield stiffness degradation and subsequent densification-induced stiffening toward the modulus of the fully dense material.

In this study, a unified stiffness evolution model is established to describe the nonlinear evolution of the elastic modulus in FDM-fabricated honeycombs during compression. Section 2 presents the theoretical formulation of the proposed stiffness evolution model. Section 3 describes the materials, geometric design, fabrication of regular hexagonal and re-entrant honeycombs, and the experimental arrangements for uniaxial compression with incremental loading–unloading protocols. Section 4 analyzes the experimental results, including the definition of mechanical properties, global stress–strain responses, evolution of the global elastic modulus, and a phenomenological constitutive equation, together with the observed deformation characteristics. In Section 5, model predictions are validated via experimental results, and the mechanisms governing anisotropic stiffness evolution are discussed, with particular emphasis on the influence of cell-wall thickness. Finally, the main findings are summarized in Section 6.

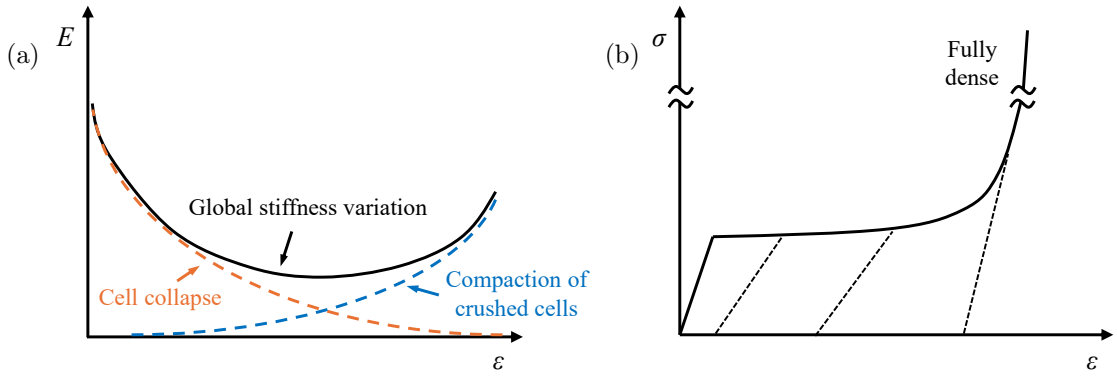

Figure 1: Stiffness evolution in cellular solids under uniaxial compression: (a) Schematic illustration showing the competition between stiffness degradation associated with cell collapse and hardening linked to compaction of crushed cells; (b) Classic stress–strain response of cellular solids highlighting the evolution of the elastic modulus, where the global stiffness is expected to converge toward that of the fully dense constituent material upon complete densification.

2. Stiffness evolution model

In this section, a stiffness evolution model is formulated by accounting for cell collapse and progressive densification within the honeycomb structure. It is well established that, for cellular solids such as honeycombs and foams, the elastic modulus decreases after yielding due to cell wall buckling, collapse, and the accumulation of structural damage, which is commonly referred to as stiffness degradation [25, 29]. However, recent experimental observations have indicated that the elastic modulus may increase with increasing compressive deformation, as a result of enhanced cell wall interactions and progressive contact between opposing cell faces. Therefore, during uniaxial compression, the elastic modulus of honeycomb structures is expected to exhibit a nonlinear evolution characterized by an initial reduction followed by a subsequent increase, rather than a purely monotonic degradation [33].

To establish the proposed evolution model, the deformation pattern of the honeycomb is assumed to be governed by a localized crush-band mode. Under this deformation mode, cells within the crush band are progressively compacted and densified, as schematically illustrated in Fig. 2. For a compressible rectangular specimen $ABCD$, as illustrated in Fig. 2(a), the global elastic modulus E during deformation is defined as

$$E = \frac{\sigma}{\varepsilon^e} = \frac{Yh}{\varepsilon^e}, \tag{1}$$

where σ denotes the macroscopic stress, ε^e represents the total elastic strain, Y is the initial yield stress, and h is a strain-dependent function introduced to characterize the strain hardening effect. The evolution of the elastic modulus is subsequently examined through three distinct deformation stages.

2.1. Stage I: Linear elastic regime ($\varepsilon \leq \varepsilon_Y$)

In the initial stage of deformation, the cellular structure is assumed to remain within the linear elastic regime, which is characterized by a constant initial modulus E_0. The deformation is considered spatially uniform until the applied strain ε reaches the initial yield strain ε_Y. The yield strain is defined as the ratio of the initial yield stress to the initial elastic modulus, namely $\varepsilon_Y = Y/E_0$. Within this regime, the elastic modulus remains constant and is expressed as

$$E = E_0, \quad \text{for } \varepsilon \leq \varepsilon_Y. \tag{2}$$

The linear elastic response terminates at $\varepsilon = \varepsilon_Y$, where the onset of structural collapse is initiated.

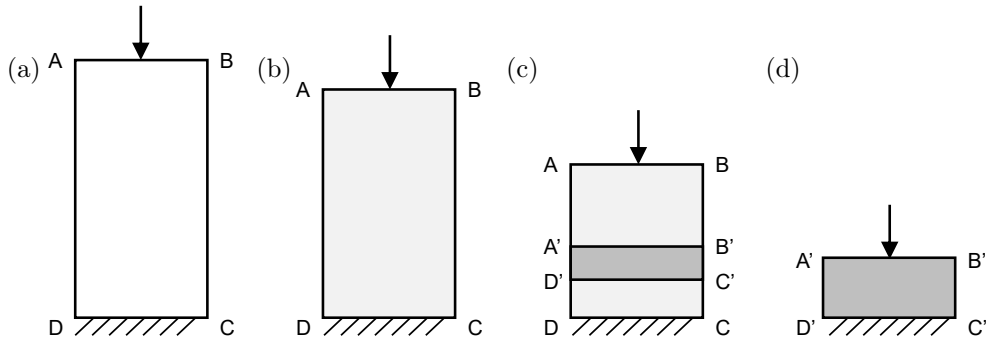

Figure 2: Schematic representation of the analytical model for the evolution of the elastic modulus: (a) initial configuration of the cellular solid specimen $ABCD$ under uniaxial compression; (b) Stage I: linear elastic regime characterized by uniform deformation; (c) Stage II: formation and propagation of a localized crush band denoted by $A'B'C'D'$; (d) Stage III: densification regime where cell-wall contact occurs.

2.2. Stage II: Coexistence of crushed and non-crushed regimes ($\varepsilon_Y < \varepsilon < \varepsilon_D$)

Upon further compression, deformation becomes spatially heterogeneous and localized crush bands are formed, represented schematically by the region $A'B'C'D'$. Within these bands, the local strain reaches the densification strain ε_D. The remainder of the specimen is considered to remain in the non-crushed regime, where the initial yield condition is maintained and the local strain is equal to ε_Y. As compression proceeds, the crushed region progressively expands, whereas the non-crushed region correspondingly diminishes. The extent of localization is quantified by introducing a dimensionless parameter λ, defined as the ratio between the height of the crushed zone and the total height of the initial sample (L). Consequently, the heights of the crushed and non-crushed regions, denoted by L_D and L_Y, respectively, are obtained from geometric compatibility and strain partitioning as

$$L_D = \lambda L = \frac{\varepsilon - \varepsilon_Y}{\varepsilon_D - \varepsilon_Y} L, \qquad L_Y = (1-\lambda)L = \frac{\varepsilon_D - \varepsilon}{\varepsilon_D - \varepsilon_Y} L. \tag{3}$$

To determine the strain-dependent elastic modulus $E(\varepsilon)$ within this regime, the total elastic strain ε^e must first be evaluated. Both regions contribute to the macroscopic elastic deformation. The elastic strain in the crushed zone is expressed as

$$\varepsilon_D^e = \varepsilon_D - \varepsilon_D^p, \tag{4}$$

where ε_D^p denotes the accumulated plastic strain at the densification state. In contrast, the elastic strain within

the non-crushed zone, which remains at the yield condition, is given by

$$\varepsilon_Y^e = \varepsilon_Y. \tag{5}$$

The total elastic strain is obtained from a volume-weighted average of the elastic contributions from the crushed and non-crushed regions. By incorporating the geometric relations in Eq. (3), the macroscopic elastic strain is written as

$$\varepsilon^e = \lambda \varepsilon_D^e + (1-\lambda)\varepsilon_Y. \tag{6}$$

Substitution of Eq. (6) into Eq. (1) yields the stiffness evolution law in Stage II,

$$E(\varepsilon) = \frac{Yh(\varepsilon)}{\lambda(\varepsilon)\varepsilon_D^e + \big(1-\lambda(\varepsilon)\big)\varepsilon_Y}, \quad \text{for } \varepsilon_Y < \varepsilon < \varepsilon_D. \tag{7}$$

2.3. Stage III: Post-densification regime ($\varepsilon \geq \varepsilon_D$)

When the applied strain exceeds the densification strain, the cellular architecture is considered fully compacted and the deformation transitions to a quasi-solid response. In this regime, localized collapse ceases and the deformation becomes spatially uniform. The stiffness evolution is no longer governed by structural degradation but is predominantly controlled by the intrinsic strain-hardening behavior described by $h(\varepsilon)$. For $\varepsilon > \varepsilon_D$, the hardening function $h(\varepsilon)$ increases rapidly in magnitude. In contrast, the variation of the elastic strain does not exhibit a comparable order-of-magnitude change. The elastic strain within the specimen in this regime cannot be rigorously derived from simple kinematic assumptions. Therefore, it is assumed that the elastic strain can be approximated by its value at the onset of densification (ε_D^e). By setting $\lambda = 1$, the elastic modulus in this regime is obtained as

$$E(\varepsilon) = \frac{Yh(\varepsilon)}{\varepsilon_D^e}, \quad \text{for } \varepsilon \geq \varepsilon_D. \tag{8}$$

The proposed stiffness evolution framework provides a unified description of the linear elastic response prior to yielding, the stiffness degradation induced by localized cell collapse after yielding, and the subsequent stiffness recovery associated with strain hardening. The model is therefore capable, at the theoretical level, of capturing the nonlinear decrease–increase trend of the elastic modulus observed experimentally. In addition, the formulation satisfies the physically required boundary condition that the elastic modulus in the fully densified state significantly exceeds its initial value. When the hardening function $h(\varepsilon)$ is omitted, the present model degenerates into a conventional formulation that accounts solely for stiffness degradation, as reported by Flores-Johnson et al. [25]. The proposed framework thus extends existing approaches by incorporating both structural collapse and intrinsic hardening within a consistent theoretical structure.

3. Materials and experimental methods

3.1. Design and fabrication of honeycombs

In this study, two cellular topologies were selected and parameterized to enable a controlled investigation of stiffness evolution associated with progressive collapse and densification: the regular hexagonal honeycomb (HC) and the re-entrant honeycomb with negative Poisson's ratio (NHC). The relative density was primarily regulated through the cell-wall thickness, for which three nominal values were prescribed ($t = 0.4$ and 0.8 mm), while all other geometric parameters were maintained constant within each topology. For the HC structure, the unit cell was defined by a uniform wall length of $a = 2.0$ mm. For the NHC structure, the unit cell consisted of a vertical wall length of 4.0 mm and an inclined wall length of 2.0 mm, with the re-entrant angle specified as 60° relative to the vertical direction. To minimize boundary effects associated with incomplete edge cells, the integrity of boundary cells was preserved to the greatest extent possible. The overall specimen dimensions were fixed at $36 \times 38 \times 12$ mm^3 for all configurations, as illustrated in Fig. 3.

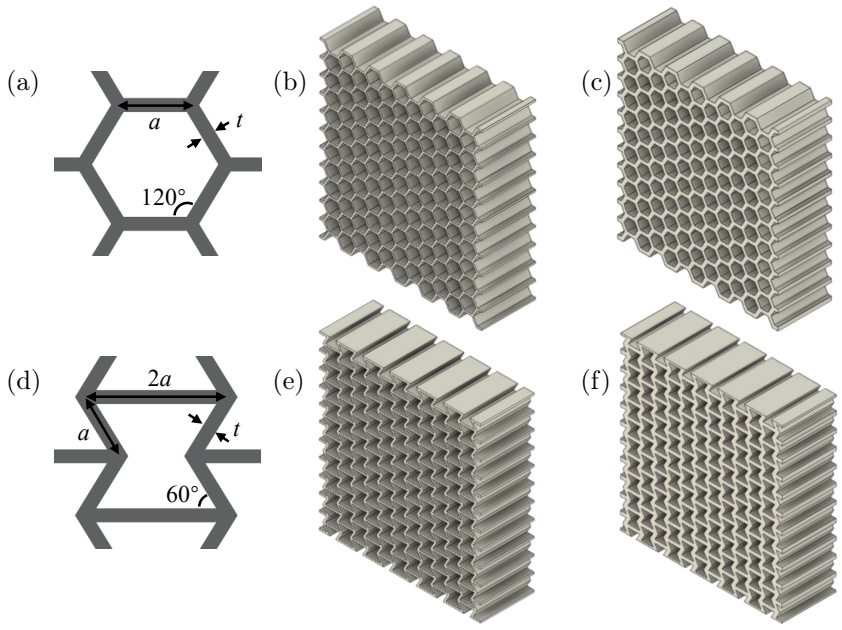

Figure 3: Geometric configurations and 3D-printed specimens of the investigated honeycombs: (a) Design parameters and dimensions of the regular hexagonal cell; (b–c) Hexagonal honeycomb structures with varying cell-wall thicknesses (t) of 0.4 mm and 0.8 mm, respectively; (d) Design parameters and dimensions of the re-entrant (auxetic) cell; (e–f) Re-entrant honeycomb structures with cell-wall thicknesses (t) of 0.4 mm and 0.8 mm, respectively.

All specimens were fabricated using Fused Deposition Modeling (FDM) on a Raise3D Pro2 platform with PolyMax^{TM} PLA filaments. The printing direction was prescribed along the out-of-plane thickness direction for all specimens to ensure consistency in the build strategy. Under this configuration, the in-plane cell walls were deposited with layer stacking oriented through the thickness, and an identical printing orientation was maintained for all topologies and thickness levels. This build orientation was selected to minimize variability associated with layer stacking effects. Consequently, variations in the measured mechanical response were primarily attributed to differences in cell geometry and nominal wall thickness rather than to changes in printing direction. The principal fabrication parameters are summarized in Table 1.

Table 1: FDM fabrication parameters for honeycomb specimens.

Extruder temp.	Bed temp.	Layer thickness	Extrusion width	Printing speed
205 °C	55 °C	0.20 mm	0.25 mm	60 mm/s

3.2. Experimental arrangements for uniaxial compression

Quasi-static compression tests were conducted using a Shimadzu universal testing machine equipped with a 50 kN precision load cell. Monotonic compression was first performed at a constant nominal strain rate of 0.03 s^{-1} to establish the baseline structural response. This strain rate was selected to ensure quasi-static conditions while limiting potential strain-rate sensitivity effects on stiffness evolution. An incremental loading–unloading protocol was subsequently implemented to quantify the evolution of the global elastic modulus $E(\varepsilon)$ throughout the collapse and densification stages. The compressive force was continuously recorded by the load cell, and the displacement was measured via crosshead travel. During incremental tests, unloading–reloading cycles were introduced at fixed global displacement intervals of 2 mm. The loading parameters were kept identical to those used in monotonic tests to ensure direct comparability. A high-resolution camera was employed simultaneously to document the deformation morphology and the spatial development of localized crush bands.

4. Results

4.1. Definition of mechanical properties

Definition 1. *Initial elastic modulus* E_0 – the slope of the linear elastic region observed during the initial loading phase.

Definition 2. *Effective elastic modulus* $E(\varepsilon)$ – the elastic modulus during progressive collapse and densification, determined from the secant slope connecting the unloading point and the subsequent reloading onset at each strain level.

Definition 3. *Initial yield stress* Y – the stress at the intersection of the stress–strain curve and a line parallel to the linear elastic portion, offset by a strain of 0.2%.

Definition 4. *Energy absorption efficiency* η – the ratio of cumulative strain energy density to the instantaneous stress [46]:

$$\eta(\varepsilon) = \frac{\int_0^{\varepsilon} \sigma(\varepsilon) d\varepsilon}{\sigma(\varepsilon)}. \tag{9}$$

Definition 5. *Densification strain* ε_D – the strain at which the energy absorption efficiency attains its maximum [46], $\eta_{\max}$, indicating the onset of significant cell compaction, as schematically illustrated in Fig. 4.

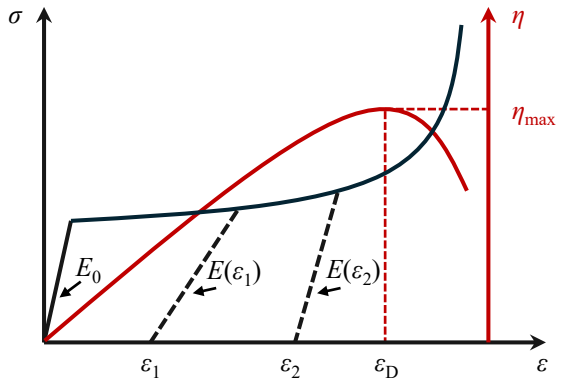

Figure 4: Schematic representation of the mechanical characterization and parameter definitions: (a) Typical stress–strain (σ–ε) trajectory exhibiting three distinct stages: linear elasticity, strain hardening, and densification; (b) Evolution of energy absorption efficiency (η) as a function of strain. The initial elastic modulus E_0 is defined by the slope of the linear region, while the effective moduli $E(\varepsilon_1)$ and $E(\varepsilon_2)$ are determined from the unloading-reloading slopes at respective strain levels. The densification strain ε_D is identified at the peak energy absorption efficiency $\eta_{\max}$, marking the transition into the compacted state.

4.2. Global stress response

4.2.1. Nominal stress–strain curves

The global nominal stress–strain curves of HC and NHC structures with cell-wall thicknesses of 0.4 mm and 0.8 mm, subjected to both monotonic and incremental cyclic uniaxial compression along the 1- and

2-directions, are presented in Fig. 5. Under uniaxial compression, all specimens exhibited a characteristic three-stage mechanical response consisting of an initial linear elastic region, a strain-hardening plateau, and a subsequent densification phase. For compression along the 2-direction, where the loading is aligned with the vertical ribs of the honeycombs, a distinct stress drop was observed after yielding due to localized structural crushing. This phenomenon was more pronounced in NHC structures.

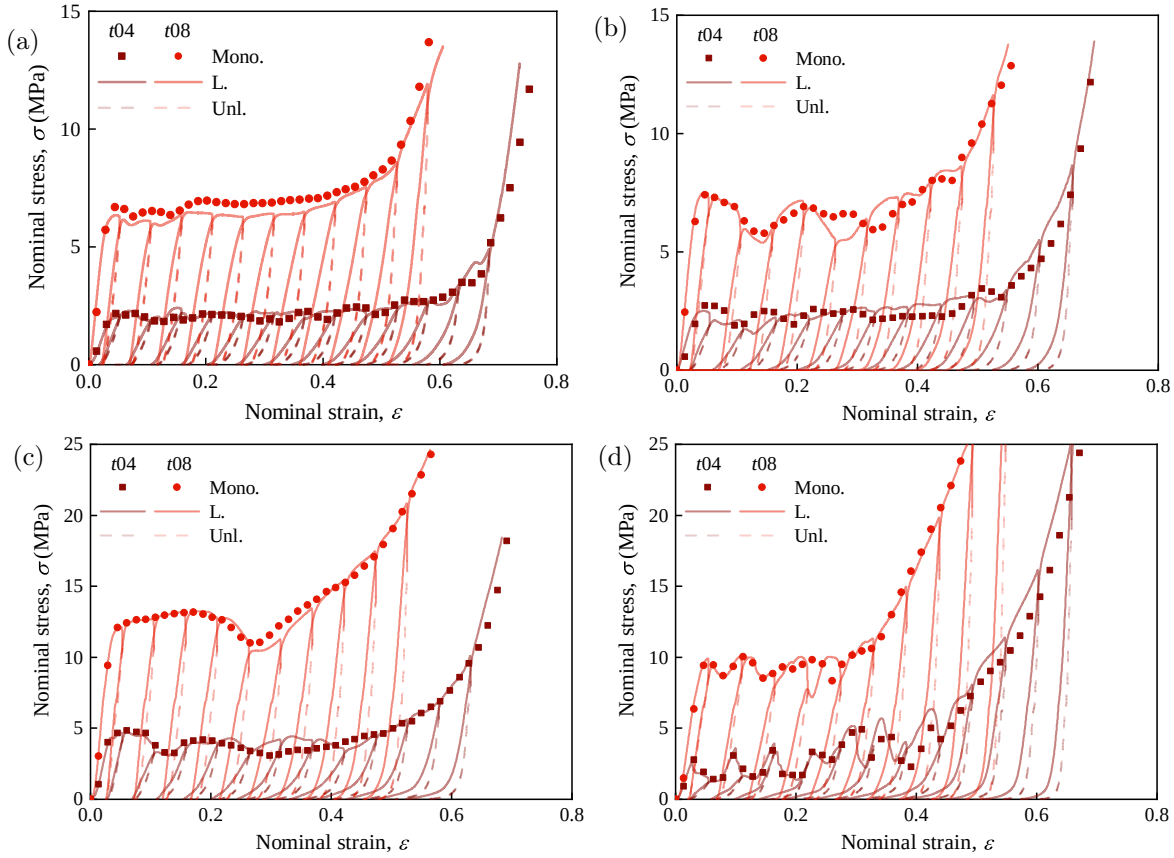

Figure 5: Global stress–strain (σ–ε) responses of the cellular structures under quasi-static compression: (a) HC structure in the 1-direction; (b) HC structure in the 2-direction; (c) NHC structure in the 1-direction; (d) NHC structure in the 2-direction.

Significant differences were observed in the stress responses between specimens with different wall thicknesses. Across the entire strain range, the stress levels of structures with a wall thickness of 0.8 mm were approximately 2.5 times higher than those of the 0.4 mm thick structures. Furthermore, in specimens with greater wall thickness, the stress increased sharply at lower strains as the structures entered the densification

stage. The stress–strain trajectories obtained from incremental cyclic tests were consistent with the monotonic compression curves, confirming the reliability and repeatability of the measurements. Although hysteresis loops were present between the loading and unloading paths, indicative of energy dissipation due to localized plastic deformation and friction, these effects were neglected in the subsequent analysis, with the focus placed on the evolution of the reloading elastic modulus.

4.2.2. Evolution of the global elastic modulus

The evolution of the global elastic modulus $E(\varepsilon)$ for HC and NHC structures with wall thicknesses of 0.4 mm and 0.8 mm, compressed along the 1- and 2-directions, is presented in Fig. 5. For all specimens, a non-monotonic evolution of the elastic modulus was observed. At small strains (typically below 10%), a gradual reduction in modulus occurred, which was attributed to the initiation of localized cell-wall bending and progressive microstructural instability. As the strain increased, the modulus reached a minimum value corresponding to the onset of significant structural collapse. With further deformation, a pronounced recovery of stiffness was observed as the structures entered the densification regime. This stiffening behavior was associated with intensified cell-wall contact and compaction, leading to enhanced load transfer through the increasingly constrained cellular network. The magnitude and strain level of modulus recovery were strongly influenced by wall thickness and loading direction. Specimens with a wall thickness of 0.8 mm exhibited higher minimum moduli and earlier stiffness recovery compared with the 0.4 mm counterparts. Additionally, directional dependence was evident. Under compression along the 2-direction, where vertical ribs were aligned with the loading axis, a more abrupt reduction in modulus was observed immediately after yielding due to localized crushing bands. In contrast, loading along the 1-direction led to a more gradual stiffness degradation process. The evolution of the elastic modulus was therefore closely related to the underlying deformation mechanisms, as further discussed in Section 5.2.

4.2.3. Phenomenological constitutive equation

To explicitly characterize the evolution of the elastic modulus within the theoretical framework established in Section 2, the experimental stress–strain trajectories were fitted using an adapted constitutive formulation. Based on one-dimensional stress wave theory, Zheng et al. [48, 49] derived the rigid–plastic hardening (R–PH) relationship, in which the hardening law was expressed as $\sigma \propto C\varepsilon/(1-\varepsilon)^2$, where C denotes the strain-hardening parameter. This formulation was subsequently refined to $\sigma \propto C\varepsilon/(\varepsilon_m - \varepsilon)^2$ to more accurately describe the transition from the plateau regime to densification [50, 52], where ε_m corresponds to the maximum attainable

strain. In the present study, since the evolution of both the initial and post-yield elastic moduli constituted the primary focus, the cellular structures were not idealized as rigid–plastic materials. Instead, a linear elastic response was incorporated prior to yielding. A phenomenological expression derived from the R–PH relationship was therefore adopted to describe the complete stress–strain response of the honeycombs, given by

$$\sigma = \begin{cases} E_0 \varepsilon, & \varepsilon < \varepsilon_Y, \\ Y\left(1 + \dfrac{C(\varepsilon - \varepsilon_Y)}{(\varepsilon_m - (\varepsilon - \varepsilon_Y))^2}\right), & \varepsilon \geq \varepsilon_Y. \end{cases} \tag{10}$$

The experimental stress–strain trajectories of HC and NHC structures with different wall thicknesses and loading directions were fitted using Eq. (10). A comparison between the measured data and the fitted curves is shown in Fig. 6. Reasonable agreement was obtained, demonstrating that the proposed phenomenological model accurately reproduced the plateau response and the subsequent rapid hardening associated with densification. The hardening parameters extracted from these fittings provided essential inputs for the analytical model developed in Section 5.1, which was subsequently employed to predict the evolution of the effective elastic modulus during compression.

4.3. Deformation characteristics

The residual (irrecoverable) deformation characteristics of HC and NHC structures, captured after unloading from specified displacements during incremental cyclic compression, are illustrated in Figs. 7 and 8. As shown in Fig. 7(a), the HC structure with a wall thickness of 0.4 mm under 1-direction loading (loading parallel to the inclined ribs) exhibited distinct inclined crush bands. Within these localized regions, deformation was primarily governed by cell-wall bending. A residual crush band was clearly observed after unloading from a displacement of 4 mm (corresponding to 10.5% strain). Upon subsequent compression, the localized deformation progressed through the propagation of these crush bands, ultimately leading to gradual densification beyond a displacement of 22 mm (57.9% strain). In contrast, the crush bands formed under 2-direction loading (loading parallel to the vertical ribs), shown in Fig. 7(b), were dominated by cell-wall buckling and fracture, with a slightly broader spatial distribution than those observed under 1-direction loading. When the wall thickness was increased to 0.8 mm, the deformation characteristics under 1-direction loading remained qualitatively similar to those of the 0.4 mm thick specimens, as illustrated in Fig. 7(c), where inclined crush bands propagated progressively and resulted in significant densification at a displacement of 22 mm. For 2-direction loading (Fig. 7(d)), the increased wall thickness enhanced the structural toughness, thereby reducing the extent of material fracture

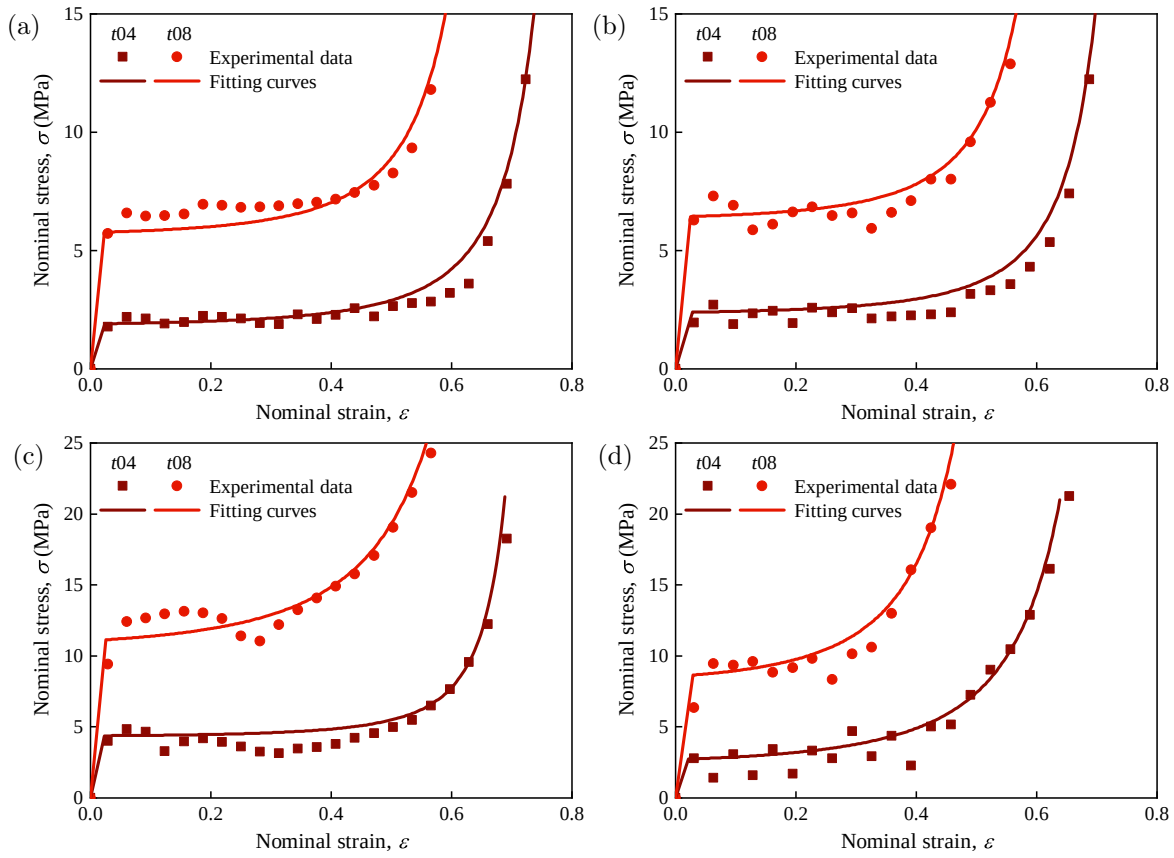

Figure 6: Fitting results obtained from the modified R–PH model: (a) HC structure in the 1-direction; (b) HC structure in the 2-direction; (c) NHC structure in the 1-direction; (d) NHC structure in the 2-direction.

within localized deformation zones. Significant densification was likewise observed at a displacement of 22 mm for this configuration.

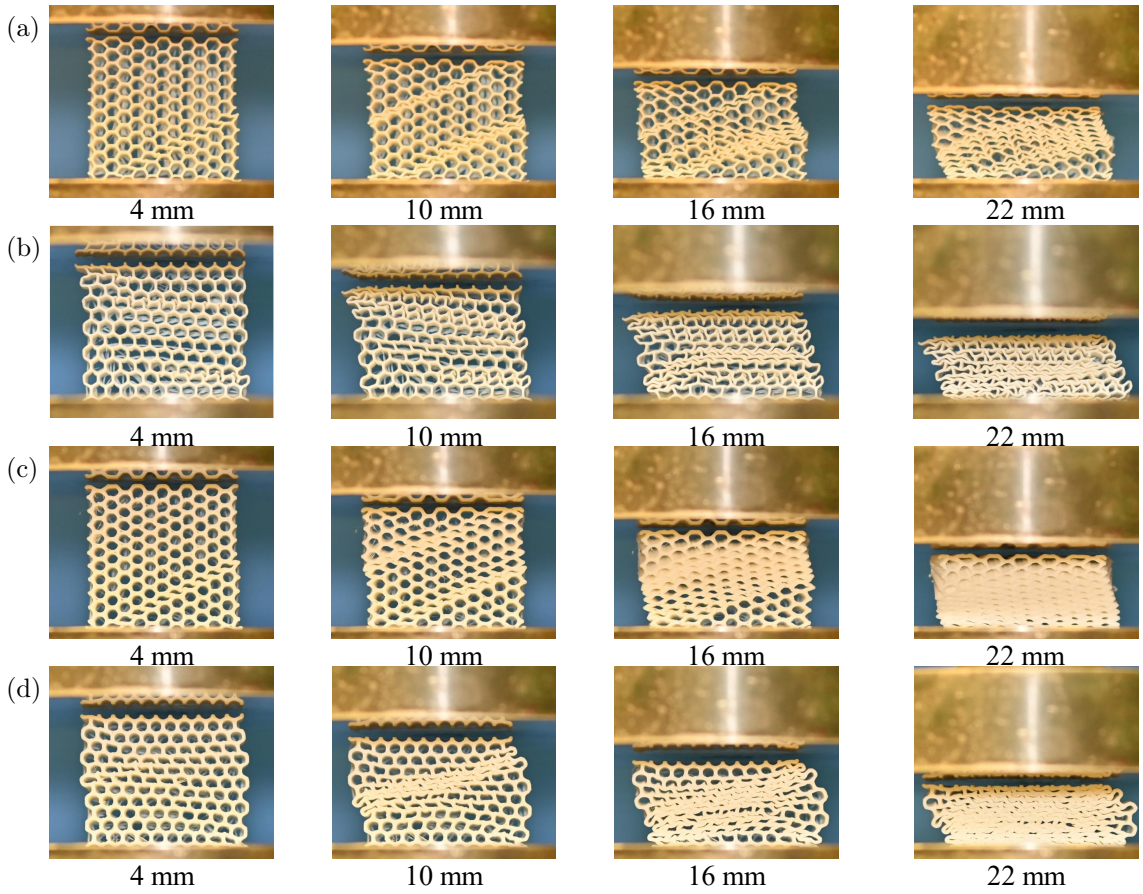

Figure 7: Representative deformation patterns and residual strain distributions of HC structures captured after unloading from a specified displacement: (a) cell-wall thickness of 0.4 mm in the 1-direction; (b) cell-wall thickness of 0.4 mm in the 2-direction; (c) cell-wall thickness of 0.8 mm in the 1-direction; (d) cell-wall thickness of 0.8 mm in the 2-direction.

The deformation of NHC structures with a wall thickness of 0.4 mm, shown in Fig. 8, clearly demonstrated auxetic behavior, characterized by a reduced specimen width compared to the corresponding HC structures. However, the 0.8 mm thick NHC specimens exhibited noticeable lateral expansion relative to the 0.4 mm counterparts, indicating that the negative Poisson's ratio effect diminished with increasing wall thickness. Under 1-direction loading (loading parallel to the inclined ribs), the 0.4 mm thick NHC structure developed two sets of mutually inclined crush bands, resulting in an asymmetric edge profile rather than the idealized symmetric

re-entrant deformation. This behavior was consistent with previously reported numerical simulations and experimental observations [57]. In the 1-direction, deformation within the NHC crush bands was dominated by cell-wall bending without evident fracture, whereas 2-direction loading produced horizontal crush bands governed primarily by cell-wall failure. The deformation modes of the 0.8 mm thick NHC structures were qualitatively similar to those of the 0.4 mm specimens but reached densification at smaller displacements (less than 22 mm). These localized deformation features, particularly the concentration and propagation of strain at the boundaries of crush bands, provided experimental support for the fundamental assumptions of the analytical framework established in Section 2.

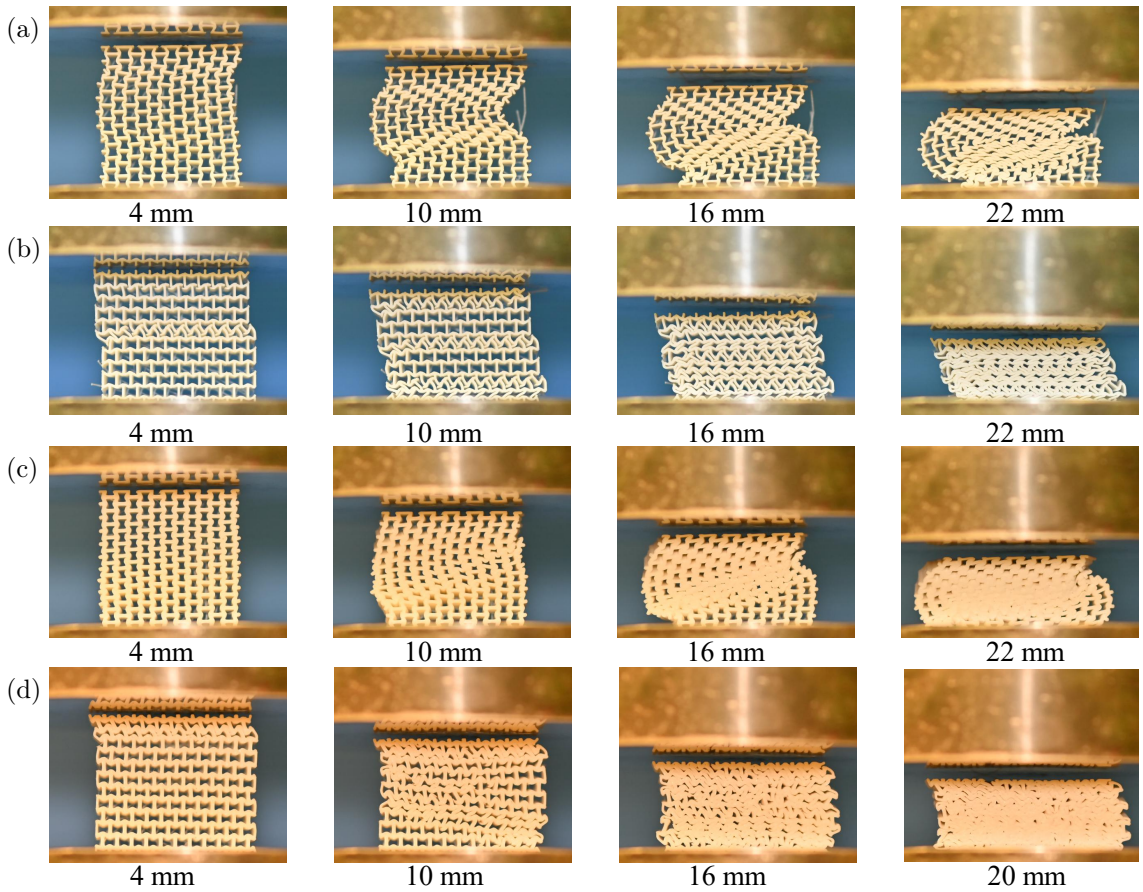

Figure 8: Representative deformation patterns and residual strain distributions of NHC structures captured after unloading from a specified displacement: (a) cell-wall thickness of 0.4 mm in the 1-direction; (b) cell-wall thickness of 0.4 mm in the 2-direction; (c) cell-wall thickness of 0.8 mm in the 1-direction; (d) cell-wall thickness of 0.8 mm in the 2-direction.

5. Discussion

5.1. Validation of the stiffness evolution model

The evolution of the global elastic modulus $E(\varepsilon)$ throughout deformation was extracted from the incremental loading–unloading experiments for both HC and NHC structures along the 1- and 2-directions, as shown in Fig. 9. The corresponding model parameters are summarized in Table 2. A pronounced non-monotonic trend was observed, in which the in-plane compressive modulus decreased after initial yielding and subsequently increased at larger strains. This behavior was intrinsically linked to the progressive deformation of the honeycomb cells. Specifically, the initial reduction in stiffness was attributed to cell-wall fracture and material softening, which degraded the load-bearing capacity of the cellular framework. In addition, as postulated in Section 2, the emergence of localized crush bands after yielding reduced the effective elastic modulus from a structural mechanics perspective. With increasing compressive strain, intensified mutual contact and compaction between cell walls enhanced stress transfer across the cellular network, resulting in a marked recovery of the global elastic modulus.

Table 2: Identified parameters of the proposed stiffness evolution model for HC and NHC structures.

Specimen	E_0 (MPa)	Y (MPa)	ε_Y	ε_D	ε_D^e
HC04-1ax	80.52	1.91	0.024	0.508	0.103
HC04-2ax	98.64	2.39	0.028	0.499	0.088
HC08-1ax	248.36	5.78	0.023	0.474	0.070
HC08-2ax	250.51	6.44	0.025	0.465	0.088
NHC04-1ax	191.70	4.38	0.023	0.524	0.110
NHC04-2ax	126.46	2.73	0.022	0.431	0.156
NHC08-1ax	442.32	11.14	0.025	0.476	0.079
NHC08-2ax	302.15	8.66	0.022	0.372	0.072

The evolution equations derived in Section 2, formulated on the basis of idealized crushing modes, were shown to reproduce the experimentally measured elastic modulus trajectories for both HC and NHC specimens with wall thicknesses of 0.4 mm and 0.8 mm. Although the predicted modulus values were slightly overestimated immediately after yielding, primarily due to the omission of material damage effects, the model successfully described the overall non-monotonic evolution, including stiffness degradation induced by

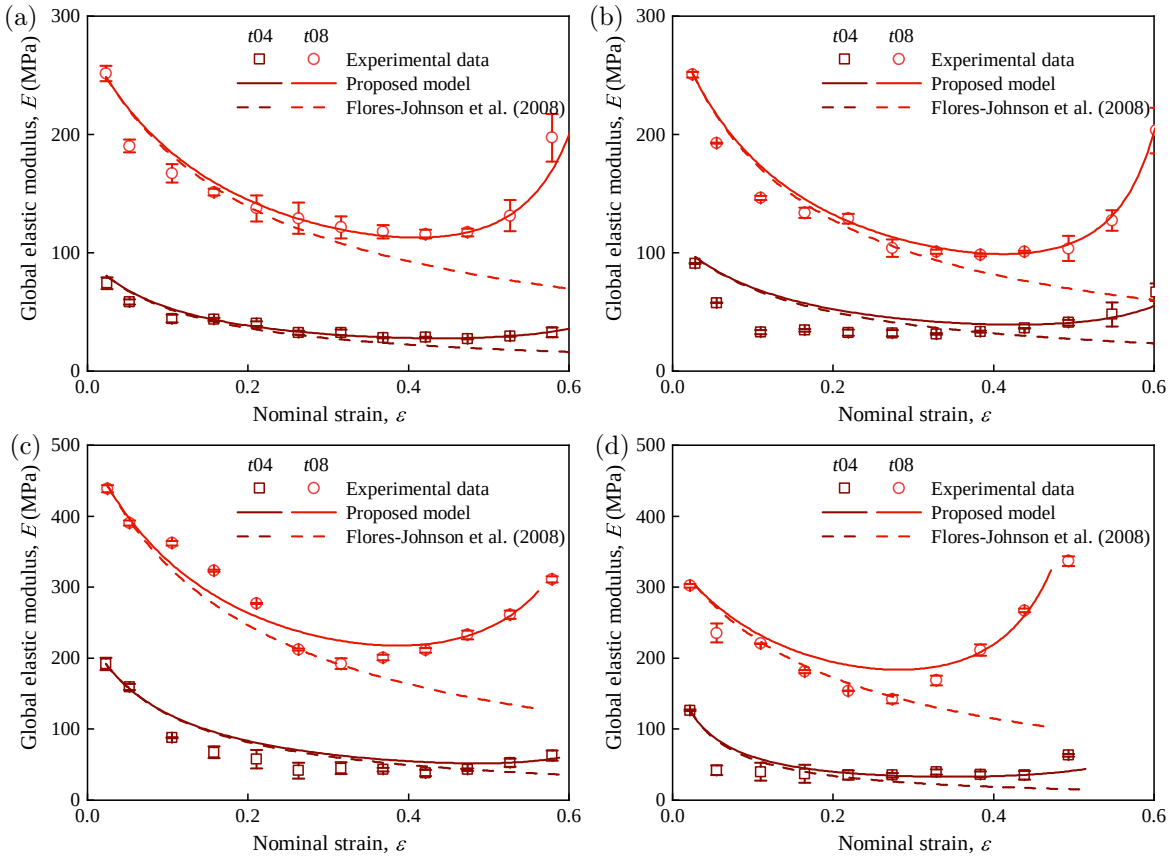

Figure 9: Evolution of the global elastic modulus $E(\varepsilon)$ during the compression process and comparison with theoretical predictions: (a) HC structures with 0.4 mm and 0.8 mm wall thicknesses in the 1-direction; (b) HC structures with 0.4 mm and 0.8 mm wall thicknesses in the 2-direction; (c) NHC structures with 0.4 mm and 0.8 mm wall thicknesses in the 1-direction; (d) NHC structures with 0.4 mm and 0.8 mm wall thicknesses in the 2-direction. The experimental data are compared with the predictions from the proposed model and the conventional model by Flores-Johnson et al. [25].

localized deformation and subsequent stiffness recovery associated with hardening and densification. In contrast, the conventional formulation proposed by Flores-Johnson et al. [25] is generally restricted to predicting stiffness degradation after yielding and does not account for the subsequent recovery stage. As the global compressive strain exceeded 20%, predictions obtained from this traditional model became markedly lower than the experimental measurements, since the strengthening contribution arising from progressive cell-wall contact and compaction was entirely neglected. The present framework therefore provides a more physically consistent and comprehensive representation of the mechanical response over the full compression regime.

5.2. Mechanisms of anisotropic stiffness evolution

The evolution of the elastic modulus exhibits pronounced anisotropy, which is fundamentally rooted in the directional dependency of the cell-wall alignment and the resulting collapse sequences. Quantitative comparison between the loading directions reveals that the stiffness reaches its minimum value significantly earlier in the 2-direction (loading parallel to the vertical ribs) than in the 1-direction. For instance, in the HC specimens with 0.4 mm wall thickness, the minimum effective modulus in the 2-direction is observed at a strain of approximately 47%, whereas the corresponding minimum in the 1-direction is delayed until 11%. This trend is consistently observed across both HC and NHC structures, indicating a common underlying mechanistic origin related to structural orientation. The earlier occurrence of the stiffness minimum in the 2-direction is primarily associated with the premature fracture of the inclined cell walls under axial compression along the straight edges (see Figs. 10 and 11). While the vertical ribs mainly act as axially compressed members, the inclined walls undergo bending-dominated deformation accompanied by stress concentration, which triggers localized failure and accelerates the degradation of the global stiffness. In contrast, loading in the 1-direction promotes a more distributed bending-dominated deformation mode, which allows for a more gradual reduction in the effective modulus.

Furthermore, the localized fracture of the inclined cell walls under 2-direction loading promotes a fragmentation-assisted crushing mechanism. This collapse mode, accompanied by progressive breakage of the cell-wall material, leads the elastic modulus to enter a minimum value shortly after yielding and subsequently evolve in a relatively stable manner. Interestingly, the fragmentation of the inclined walls induces inward contraction of the cell-wall segments (see Figs. 10 and 11), which enhances the degree of compaction within the unit cells and suppresses the lateral deformation of the specimen.

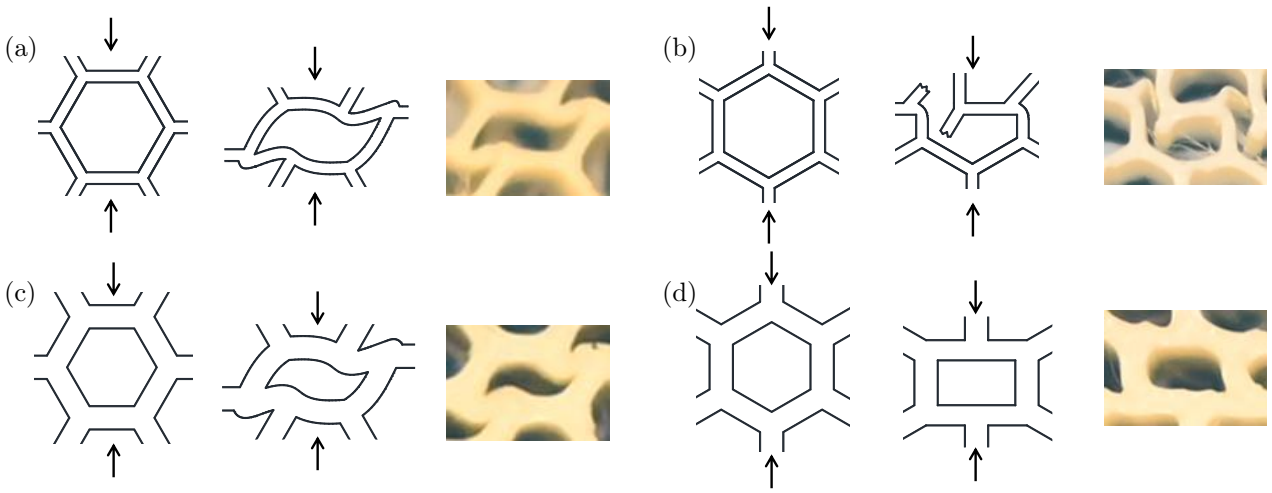

Figure 10: Influence of loading orientation and cell-wall thickness on the deformation mechanisms of HC unit cells: (a) thickness of 0.4 mm in the 1-direction; (b) thickness of 0.4 mm in the 2-direction; (c) thickness of 0.8 mm in the 1-direction; (d) thickness of 0.8 mm in the 2-direction.

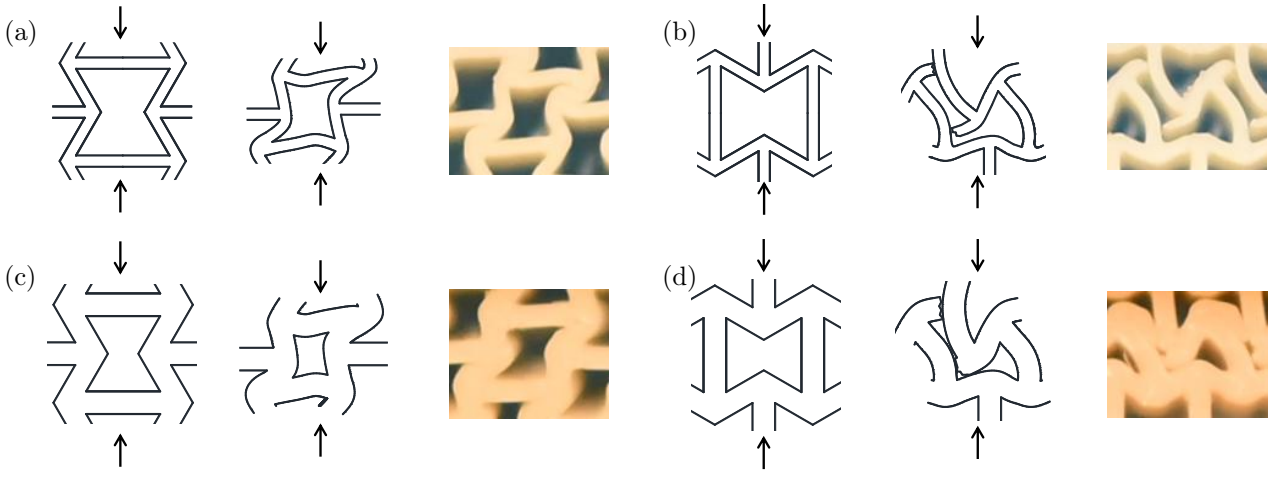

Figure 11: Influence of loading direction and cell-wall thickness on the deformation mechanisms of NHC unit cells: (a) thickness of 0.4 mm in the 1-direction; (b) thickness of 0.4 mm in the 2-direction; (c) thickness of 0.8 mm in the 1-direction; (d) thickness of 0.8 mm in the 2-direction.

5.3. Influence of cell-wall thickness

The cell-wall thickness t plays a fundamental role in determining both the magnitude and the evolution of the elastic modulus. In general, increasing the wall thickness leads to a higher effective modulus throughout the compression process due to the enhanced structural rigidity and relative density. However, the influence of thickness on the evolution trajectory of the modulus is loading-direction dependent. Owing to the distinct collapse mechanisms activated under the two in-plane orientations, the manner in which thickness modifies the onset of stiffness degradation and recovery differs between the 1- and 2-directions.

On the one hand, under 1-direction compression, the collapse process is predominantly bending-dominated. As the wall thickness increases, the flexural rigidity of the cell walls is enhanced, promoting earlier contact and compaction between adjacent cell-wall segments during progressive folding. Consequently, the rebound of the elastic modulus occurs at a lower compressive strain for thicker-walled specimens. Specifically, when the wall thickness increases from 0.4 mm to 0.8 mm, the strain corresponding to the modulus recovery in HC structures decreases from 47% to 42%, while in NHC structures it decreases from 42% to 32%. This behavior indicates that, in bending-controlled collapse, increased relative density accelerates the onset of densification.

On the other hand, under 2-direction compression, the collapse mechanism is governed primarily by fracture-dominated crushing of the inclined cell walls. Increasing the wall thickness enhances both the structural strength and the apparent toughness of the struts, thereby delaying fragmentation and the associated loss of load-carrying capacity. As a result, the strain corresponding to the rebound of the elastic modulus shifts to higher values with increasing wall thickness. When the wall thickness increases from 0.4 mm to 0.8 mm, the strain at modulus recovery in HC structures increases from $11x$% to 38%, while in NHC structures it increases from 22% to 27%.

These contrasting trends highlight that the densification strain is not solely governed by relative density, but is strongly coupled with the dominant deformation mechanism. In bending-dominated collapse (1-direction), thickness accelerates compaction, whereas in fracture-dominated collapse (2-direction), thickness delays stiffness recovery by postponing structural fragmentation.

6. Conclusions

This study proposes a unified stiffness evolution model to describe the variation of the effective elastic modulus in honeycomb structures under quasi-static uniaxial compression. The model is established from incremental loading–unloading experiments on regular hexagonal (HC) and re-entrant (NHC) honeycombs with different wall thicknesses in two orthogonal in-plane directions. The framework captures the complete modulus

evolution, including post-yield degradation and subsequent recovery due to structural compaction, and clarifies the structural origins of anisotropic stiffness behavior. The key findings are summarized as follows:

The global stress–strain response of both HC and NHC structures exhibits three stages: an initial linear elastic regime, a collapse plateau, and a densification stage with rapid modulus recovery. Incremental cyclic tests reveal a non-monotonic modulus evolution characterized by an initial decrease followed by recovery, strongly influenced by loading direction and wall thickness.

The proposed stiffness evolution model accurately predicts both stiffness degradation after yielding and recovery during densification. A minor modification of the rigid–plastic hardening (R–PH) framework introduces a linear elastic pre-yield response for quantitative fitting of the stress–strain curves. The model captures the complete non-monotonic evolution of the elastic modulus during compression, characterized by an initial decrease due to localized collapse followed by a subsequent increase driven by structural compaction. In contrast, conventional models (e.g., Flores-Johnson et al. [25]) account only for post-yield degradation and neglect modulus recovery.

Pronounced anisotropy in stiffness evolution arises from the distinct collapse mechanisms activated under the two loading directions, and this effect is further modulated by wall thickness. Under 1-direction compression, where collapse is bending-dominated, increasing wall thickness enhances flexural rigidity and promotes earlier contact and compaction of cell walls, leading to an earlier modulus recovery. In contrast, under 2-direction compression, where collapse is governed by fragmentation of inclined cell walls, thicker specimens exhibit improved strength and toughness, which delays structural breakage and shifts the onset of modulus recovery to higher strains.

Overall, this study establishes a mechanism-informed framework linking geometry, thickness, and loading orientation to anisotropic stiffness evolution. Although fracture was not explicitly modeled, the phenomenological approach provides predictive capability for the design and optimization of cellular materials under quasi-static compression.

References

[1] X. Niu, F. Xu, Z. Zou, Y. Zhu, Impact resistance of horsetail bio-honeycombs, International Journal of Mechanical Sciences 266 (2024) 108988.

[2] J. Pan, Q. Zhang, M. Li, J. Cai, A novel misplaced reinforced honeycomb with in-plane bidirectional enhancement, International Journal of Mechanical Sciences 270 (2024) 109088.

[3] X. Hu, K. Yan, H. Wu, S. Qi, M. Yuan, Dynamic response of cylindrical sandwich panels with coaxial and concentric honeycombs under blast loads, Engineering Structures 343 (2025) 120942.

[4] X. Wang, Z. Li, H. Hao, W. Chen, Experimental study on energy absorption performance of kirigami-modified honeycomb module for crash cushion, Engineering Structures 353 (2026) 122227.

[5] X. Niu, F. Xu, Z. Zou, Y. Zhu, L. Duan, Z. Du, H. Ma, Mechanical properties of horsetail bio-inspired honeycombs under quasi-static axial load, International Journal of Mechanical Sciences 260 (2023) 108663.

[6] P. Guan, N. Hao, P. Wang, Compressive behavior of 3d printed biomechanically inspired helicoidal honeycomb structures, International Journal of Mechanical Sciences (2025) 110883.

[7] X. Zhou, N. Xia, H. Liu, J. Zhang, L. Ren, L. Ren, Bio-inspired variant honeycomb structures via 4d printing: Revolutionizing the realm of energy absorption, Engineering Structures 342 (2025) 120931.

[8] Q. Hu, G. Lu, N. Hameed, K. M. Tse, Dynamic compressive behaviour of shear thickening fluid-filled honeycomb, International Journal of Mechanical Sciences 229 (2022) 107493.

[9] Y. Chen, Potential auxetic honeycomb system constructed from a new re-entrant block, Engineering Structures 340 (2025) 120718.

[10] Z. Lu, Z. Wu, J. Xu, Z. Li, Designable waveguides based on topological insulators in honeycomb sandwich panels, Engineering Structures 345 (2025) 121439.

[11] B. Wang, X. Feng, X. Wu, Z. Meng, G. Dong, J. Ding, Q. Wu, Enhanced in-plane impact characteristics of a novel circular-reinforced sinusoidal honeycomb, Engineering Structures 345 (2025) 121430.

[12] Y. He, Z. Bi, T. Wang, L. Wang, G. Lu, Y. Cui, K. M. Tse, Design and mechanical properties analysis of hexagonal perforated honeycomb metamaterial, International Journal of Mechanical Sciences 270 (2024) 109091.

[13] Y. He, G. Lu, T. Wang, L. Wang, K. M. Tse, Optimized hexagonal perforated honeycomb–chiral metamaterial for multidirectional energy absorption, International Journal of Mechanical Sciences 301 (2025) 110521.

[14] L. J. Gibson, M. F. Ashby, G. Schajer, C. Robertson, The mechanics of two-dimensional cellular materials, Proceedings of the Royal Society of London. A. Mathematical and Physical Sciences 382 (1782) (1982) 25–42.

[15] L. J. Gibson, M. F. Ashby, Cellular Solids: Structure and Properties, Cambridge University Press, 1997.

[16] O. El-Khatib, S. Kumar, W. J. Cantwell, A. Schiffer, Effective elastic properties of sandwich-structured hierarchical honeycombs: An analytical solution, International Journal of Mechanical Sciences 265 (2024) 108883.

[17] J.-Y. Liu, H.-T. Liu, M.-R. An, Crushing behaviors of novel diabolo shaped honeycombs with enhanced energy absorption performance, International Journal of Mechanical Sciences 229 (2022) 107492.

[18] N. Ma, Q. Han, S. Han, C. Li, Hierarchical re-entrant honeycomb metamaterial for energy absorption and vibration insulation, International Journal of Mechanical Sciences 250 (2023) 108307.

[19] Y.-C. Li, H.-T. Liu, S. Wang, A rhombic bidirectional re-entrant honeycomb with enhanced dual-platform stress characteristics and programmable mechanical properties, Engineering Structures 346 (2026) 121676.

[20] R. Johnston, Z. Kazancı, Analysis of additively manufactured (3d printed) dual-material auxetic structures under compression, Additive Manufacturing 38 (2021) 101783.

[21] A. Farrokhabadi, H. Veisi, H. Gharehbaghi, J. Montesano, A. H. Behravesh, S. K. Hedayati, Investigation of the energy absorption capacity of foam-filled 3d-printed glass fiber reinforced thermoplastic auxetic honeycomb structures, Mechanics of Advanced Materials and Structures 30 (4) (2023) 758–769.

[22] A. Montazeri, E. Bahmanpour, M. Safarabadi, Three-point bending behavior of foam-filled conventional and auxetic 3d-printed honeycombs, Advanced Engineering Materials 25 (17) (2023) 2300273.

[23] M. Irfan, S. Patel, R. Umer, M. Ali, Y. Dong, Thermal and morphological analysis of various 3d printed composite honeycomb cores, Composite Structures 290 (2022) 115517.

[24] R. F. Faidallah, A. M. Abd-El Nabi, M. M. Hanon, Z. Szakál, I. Oldal, Compressive and bending properties of 3d-printed wood/pla composites with re-entrant honeycomb core, Results in Engineering 24 (2024) 103023.

[25] E. Flores-Johnson, Q. Li, R. Mines, Degradation of elastic modulus of progressively crushable foams in uniaxial compression, Journal of cellular plastics 44 (5) (2008) 415–434.

[26] U. E. Ozturk, G. Anlas, Energy absorption calculations in multiple compressive loading of polymeric foams, Materials & Design 30 (1) (2009) 15–22.

[27] U. E. Ozturk, G. Anlas, Finite element analysis of expanded polystyrene foam under multiple compressive loading and unloading, Materials & Design 32 (2) (2011) 773–780.

[28] U. E. Ozturk, G. Anlas, Hydrostatic compression of anisotropic low density polymeric foams under multiple loadings and unloadings, Polymer testing 30 (7) (2011) 737–742.

[29] Y. Sun, B. Amirrasouli, S. B. Razavi, Q. Li, T. Lowe, P. Withers, The variation in elastic modulus throughout the compression of foam materials, Acta Materialia 110 (2016) 161–174.

[30] M. Avalle, M. Frascio, M. Monti, An improved model to describe the repeated loading-unloading in compression of cellular materials, Procedia Structural Integrity 12 (2018) 19–31.

[31] S. Zhang, M. Liu, C. Wang, H. Zhang, J. Wu, Compression, unloading-reloading, and tension mechanical behaviors of silt-based foamed concrete under uniaxial loading, Construction and Building Materials 347 (2022) 128558.

[32] D. Qiao, B. Yang, Z. Jiang, L. Zhou, Z. Liu, Y. Liu, L. Tang, A new plastic flow theoretical model and verification for non-dense metals, Acta Mechanica Sinica 39 (9) (2023) 423085.

[33] S. Wang, H. Li, Y. Guo, V. Shim, Anisotropic post-yield and damage response of polyurethane foam compressed at different strain rates – an experimental study, International Journal of Impact Engineering (2026).

[34] Q. H. Jebur, P. Harrison, Z. Guo, G. Schubert, X. Ju, V. Navez, Characterisation and modelling of a transversely isotropic melt-extruded low-density polyethylene closed cell foam under uniaxial compression, Proceedings of the Institution of Mechanical Engineers, Part C: Journal of Mechanical Engineering Science 226 (9) (2012) 2168–2177.

[35] A. Miyase, S. S. Wang, Test method development and determination of three-dimensional strength and failure modes of polyvinyl chloride structural foams, Journal of Engineering Materials and Technology 139 (3) (2017) 031006.

[36] M. S. H. Fatt, C. Zhong, P. C. Gadepalli, X. Tong, Crushable multiaxial behavior of sandwich foam cores: Pressure vessel experiments, Journal of Sandwich Structures & Materials 23 (6) (2021) 2028–2063.

[37] D. Ben Abdeljelil, S. Chatti, R. O Ahmed Ben Ali, Effect of strain rate and load orientation on cyclic response of anisotropic polyurethane foam, Cellular Polymers 41 (4) (2022) 147–162.

[38] C. Casavola, L. Del Core, V. Moramarco, G. Pappalettera, M. Patronelli, Experimental and numerical analysis of the poisson's ratio on soft polyurethane foams under tensile and cyclic compression load, Mechanics of Advanced Materials and Structures 29 (28) (2022) 7172–7188.

[39] H. Wang, C. Zhang, T.-T. Li, H. Peng, L. Liu, J.-H. Lin, C.-W. Lou, Soft polyurethane foam reinforced by expanded polystyrene particles: Compression performance, strain rate, and cyclic compression response, Polymers for Advanced Technologies 34 (11) (2023) 3415–3425.

[40] C. Chen, T. Lu, A phenomenological framework of constitutive modelling for incompressible and compressible elasto-plastic solids, International Journal of Solids and Structures 37 (52) (2000) 7769–7786.

[41] V. S. Deshpande, N. A. Fleck, Isotropic constitutive models for metallic foams, Journal of the Mechanics and Physics of Solids 48 (6-7) (2000) 1253–1283.

[42] V. Deshpande, N. Fleck, Multi-axial yield behaviour of polymer foams, Acta materialia 49 (10) (2001) 1859–1866.

[43] V. Tagarielli, V. Deshpande, N. Fleck, C. Chen, A constitutive model for transversely isotropic foams, and its application to the indentation of balsa wood, International Journal of Mechanical Sciences 47 (4-5) (2005) 666–686.

[44] P. Li, Y. Guo, V. Shim, A constitutive model for transversely isotropic material with anisotropic hardening, International Journal of Solids and Structures 138 (2018) 40–49.

[45] P. J. Tan, S. R. Reid, J. J. Harrigan, Z. Zou, S. Li, Dynamic compressive strength properties of aluminium foams. part ii—'shock'theory and comparison with experimental data and numerical models, Journal of the Mechanics and Physics of Solids 53 (10) (2005) 2206–2230.

[46] P. J. Tan, S. R. Reid, J. J. Harrigan, Z. Zou, S. Li, Dynamic compressive strength properties of aluminium foams. part i—experimental data and observations, Journal of the Mechanics and Physics of Solids 53 (10) (2005) 2174–2205.

[47] J. J. Harrigan, S. R. Reid, A. S. Yaghoubi, The correct analysis of shocks in a cellular material, International Journal of Impact Engineering 37 (8) (2010) 918–927.

[48] Z. Zheng, J. Yu, C. Wang, S. Liao, Y. Liu, Dynamic crushing of cellular materials: A unified framework of plastic shock wave models, International Journal of Impact Engineering 53 (2013) 29–43.

[49] Z. Zheng, C. Wang, J. Yu, S. R. Reid, J. J. Harrigan, Dynamic stress–strain states for metal foams using a 3d cellular model, Journal of the Mechanics and Physics of Solids 72 (2014) 93–114.

[50] S. Wang, Z. Zheng, C. Zhu, Y. Ding, J. Yu, Crushing and densification of rapid prototyping polylactide foam: Meso-structural effect and a statistical constitutive model, Mechanics of Materials 127 (2018) 65–76.

[51] Y. Zhang, Y. Zhu, B. Chang, J. Yu, Z. Zheng, Blast-loading simulators: Multiscale design of graded cellular projectiles considering projectile–beam coupling effect, Journal of the Mechanics and Physics of Solids 180 (2023) 105402.

[52] S. Wang, Y. Zhu, J. Yu, L. Wang, Z. Zheng, Anisotropic mechanics of cell-elongated structures: Finite element study based on a 3d cellular model, Thin-Walled Structures 205 (2024) 112405.

[53] Y. Zhang, Y. Zhu, C. Gou, H. Zheng, Q. Zhou, K. Wang, T. Yu, J. Yu, Z. Zheng, Impact dynamics of graded cellular projectiles on clamped circular plates: A coupling analysis theory and verification, International Journal of Impact Engineering (2026) 105641.

[54] X. Li, Z. Lu, Z. Yang, Q. Wang, Y. Zhang, Yield surfaces of periodic honeycombs with tunable poisson's ratio, International Journal of Mechanical Sciences 141 (2018) 290–302.

[55] M. Beigrezaee, S. Jalali, D. Misseroni, N. Pugno, A refined gibson-ashby model for functionally graded honeycombs with random irregularities, International Journal of Mechanical Sciences (2026) 111297.

[56] X. Guo, E. Wang, H. Yang, W. Zhai, Mechanical characterization and constitutive modeling of additively-manufactured polymeric materials and lattice structures, Journal of the Mechanics and Physics of Solids 189 (2024) 105711.

[57] J. Liu, J. Liu, K. Gao, I. Mohagheghian, W. Fan, J. Yang, Z. Wu, A bioinspired gradient curved auxetic honeycombs with enhanced energy absorption, International Journal of Mechanical Sciences 291 (2025) 110189.